Structure, Disorder, and Molecular Dynamics in Zn(D,L-histidine)$_2$: EPR of Copper Ion Dopants, X-ray Diffraction, and Calorimetric Studies

Sergio D. Dalosto and Rafael Calvo*

Departamento de Física, Facultad de Bioquímica y Ciencias Biológicas, Universidad Nacional del Litoral and INTEC (CONICET-UNL), Güemes 3450, 3000 Santa Fe, Argentina

José L. Pizarro and María I. Arriortua

Departamento de Mineralogía y Petrología, Facultad de Ciencias, Universidad del País Vasco, Apartado 644, 48080 Bilbao, Spain

Received: September 5, 2000; In Final Form: November 16, 2000

We report EPR, X-ray crystallographic, and calorimetric measurements in copper-doped and pure Zn(II) bis(D,L-histidino)pentahydrate ($C_{12}H_{26}N_6O_9Zn$), to be called Zn(D,L-histidine)$_2$. EPR data in copper-doped single crystals were obtained at 9.8 GHz as a function of the orientation of the magnetic field **B** at 298 and 80 K, and as a function of temperature (T) for fixed orientations of **B**. Powder samples were studied at 9.8 and 35 GHz. Steep changes of the EPR spectra with temperature occur around $T_c = 268$ K. Above T_c we observe spectra arising from a single copper with rhombic $\boldsymbol{g}$ and copper hyperfine $\boldsymbol{A}$ tensors. The resonances display a strong dependence of the line width with the hyperfine component. Below T_c the spectra can be assigned to two different copper ions displaying axial symmetry and related by a C_2 rotation. As T increases approaching T_c, they collapse into the high-temperature spectrum. A peak in the differential specific heat of pure Zn(D,L-histidine)$_2$ between 235 and 270 K indicates a transition intrinsic to the host material. Full X-ray structural studies were performed at 293 and at 150 K, above and below T_c. At 293 K our results are similar to those reported before. The low-temperature data show disorder in the water molecules. We interpret the experimental results with a model where the copper atoms hop randomly between different states. This dynamics is related to the fluctuating disorder in the lattice and produces steep changes on the EPR spectra of copper ion dopants. The role of dynamic Jahn−Teller distortions is discussed. A bonding scheme for the copper ions in Zn(D,L-histidine)$_2$ is proposed, and it is compared with that encountered in type 1 blue copper proteins.

Introduction

The electron paramagnetic resonance (EPR) spectra of paramagnetic ions introduced in diamagnetic hosts provide information about the electronic structure of the magnetic ion, and about the structure and dynamics of its environment.[1] If a diamagnetic material displays a phase transition, the anomalies of the temperature dependence of the spectra allow to define characteristics of the transition.[2] EPR is also well suited to study vibronic couplings, "the bridge from electronic to nuclear motions" according Bersuker.[3] When the rates of the vibronic or dynamical Jahn−Teller couplings are similar to the frequencies characteristic of the EPR experiments, deep changes of the spectra are produced. The temperature dependences of the spectral parameters carry information about the dynamics of the coupled electronic−nuclear system. The investigation of vibronic couplings in copper ions started with the early study of a highly symmetric system by Bleaney and Ingram,[4] and was followed by studies of systems with lower symmetries performed by several authors.[3,5−12]

Metal amino acid complexes are useful to model the bonding and properties of metal ions in metaloproteins.[13] An important ligand to metal ions is the amino acid histidine, and many investigations dealing with complexes of histidine with metal ions have been reported. The crystal structures of zinc,[14,15] cobalt,[16] cadmium,[17] nickel,[18] and copper[19] complexes show the bis(histidine) as a bidentate ligand, with the metal ion bound to imidazole and amino nitrogens, and to carboxylate oxygens, in tetrahedral, square planar, or octahedral coordinations.

Because of the role as model systems for copper proteins, EPR studies of several amino acids and complexes of zinc or cadmium with amino acids dopped with copper have been performed in powder and single-crystal samples.[20−30] Rockenbauer et al.[23] reported an X-band EPR study of powdered samples and frozen solutions of copper doped Zn(D,L-histidine)$_2$ as a function of temperature. They observed an anomalous temperature dependence of the g-factor and the hyperfine coupling parameter at temperatures around 250 K, and attributed this behavior to a Jahn−Teller effect on the copper ions. The crystal structure of Zn(D,L-histidine)$_2$ at room temperature was reported by Harding and Cole,[14] who determined the positions of all atoms. They found two alternative positions for some of the water hydrogen atoms, and an underlying proton dynamics may be expected from these results.

In this work we investigated the properties of Zn(D,L-histidine)$_2$ using three techniques. We studied with great detail the changes with temperature of the EPR spectra of copper ion dopants using single-crystal samples, and also powder samples of Zn(D,L-histidine)$_2$. Differential scanning calorimetry (DSC) measurements performed in pure samples of Zn(D,L-histidine)$_2$ showed a peak in the same temperature range where the EPR

* Corresponding author. E-mail address: rafael.calvo@dfbioq.unl.edu.ar.

10.1021/jp003167n CCC: $20.00
Published on Web 01/12/2001

spectra of copper become anomalous. This indicates that some sources of the anomalies are inherent to Zn(D,L-histidine)$_2$. They are not due only to the behavior of the copper ions, but are driven by the properties of the host lattice. In order to understand these results we performed X-ray crystallographic measurements in pure crystals at 293 and 150 K. Our data indicate no change in crystallographic symmetry. However, at low temperature we observe crystallographic disorder in Zn(D,L-histidine)$_2$. We introduce a model describing simultaneously the three sources of information. We propose a hopping dynamics for the disordered atoms in the lattice and conclude that the observed anomalies on the EPR spectra reflect this disorder and dynamic Jahn−Teller distortions of the ligands to the copper sites.

Experimental Section

Sample Preparation. In a typical synthesis of Zn(D,L-histidine)$_2$, 0.62 g of D,L-histidine (4 mmol) and 0.58 g of zinc sulfate (2 mmol) are dissolved in 40 mL of water, and filtered through a Sartorius membrane of 0.2 μm pore size. A neutral pH of the solutions is obtained with NaOH. Single-crystal samples of Zn(D,L-histidine)$_2$ were obtained by evaporation of an aqueous solution at $T = 63$ °C. Copper-doped single-crystal samples of Zn(D,L-histidine)$_2$ for EPR measurements ($\sim$2 mm^3) were obtained adding copper sulfate with 0.001 Cu/Zn atomic ratio to the mixture described above.

Single crystals are elongated along the *c*-axis and display {110} crystal faces. The axes were identified measuring the angles between these lateral faces with a goniometric microscope. The samples were handled with care because they easily dehydrate in a dry environment at room temperature. Powder samples were prepared from small single crystals. A powder sample with water and amino protons replaced by deuterium was prepared from a D_2O solution.

Diffraction Data, Structure Solution, and Refinement. X-ray diffraction studies of Zn(D,L-histidine)$_2$ were performed at 293 and 150 K using an Enraf-Nonius CAD-4 diffractometer, employing Mo Kα graphite-monochromated radiation (λ = 0.71073 Å), and the $2\theta/\omega$ scan technique. The sample used in the X-rays data collection was sealed inside a thin wall glass capillary to avoid dehydration. Unit cell constants were determined by a least-squares fit of the 2θ values for 25 high angle centered reflections. At 293 K, 6347 reflections were measured ($5° < 2\theta < 60°$), 2978 of which were independent (R_{int} = 2.69%). At 150 K, 6240 reflections were measured in the same 2θ range, and 2920 were independent (R_{int} = 1.55%). The data were corrected for Lorentz and polarization effects. No absorption correction was applied. Analysis of the systematic absences suggested two possible monoclinic space groups, *C*2/*c* and *Cc*. The structure was solved with both space groups, but the refinement indicated that *C*2/*c* was the proper choice.[31]

The structure of Zn(D,L-histidine)$_2$ at 293 K was solved by Patterson methods[32] and refined on F^2 and full-matrix least-squares techniques.[33] Non-hydrogen atoms were refined with anisotropic displacement coefficients. Hydrogen atoms were located in a difference Fourier map, and included in the refinement with two common isotropic thermal parameters, one for the water hydrogen atoms, and another for the histidine hydrogen atoms. The distances O−H in the water molecules were restrained to 0.85 Å with a standard deviation of 0.03 Å. The refinement converged to $R = 3.45\%$, $wR^2 = 8.16$, and $S = 0.974$, with 169 variables and 17 reflections per refined parameter.

The coordinates derived from the study at 293 K were used as starting values in the refinement of the crystal structure at 150 K with the above-described conditions. The final coordinates for atoms other than water molecules at 150 K agreed fairly well with the results at 293 K. The main difference is the split of a water oxygen atom over two positions with site occupancies 0.5. At 150 K the refinement converged to $R = 5.24\%$, $wR^2 = 12.75$, and $S = 1.184$, with 178 variables and 16 reflections per refined parameter.

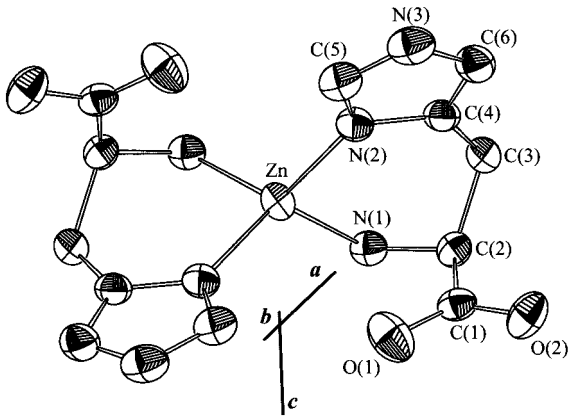

Figure 1. Zn(D,L-histidine)$_2$ molecule displaying the labeling of the atoms, as obtained at 293 K.

TABLE 1: Crystal Data for Zn(D,L-histidine)$_2$ and, for Comparison, Data Taken from Ref 14

	$T = 293$ K (ref 14)	$T = 293$ K (this work)	$T = 150$ K (this work)
empirical formula	$C_{12}H_{26}N_6O_9Zn$	$C_{12}H_{26}N_6O_9Zn$	$C_{12}H_{26}N_6O_9Zn$
formula weight	463.76	463.76	463.76
space group	*C*2/*c*	*C*2/*c*	*C*2/*c*
crystal system	monoclinic	monoclinic	monoclinic
a (Å)	16.410 (15)	16.386(1)	16.250(4)
b (Å)	14.755 (15)	14.7455(8)	14.644(2)
c (Å)	10.990 (15)	10.9739(8)	10.907(2)
β (°)	129.60 (15)	129.594(5)	129.46(2)
Z	4	4	4
V (Å^3)	2050.3	2043.2(2)	2003.9(7)
D_{calc} (mg/m^3)	1.502	1.508	1.537

Crystallographic results at both temperatures are listed in Table 1 which includes the results of Harding and Cole.[14] Figure 1 displays an ORTEP projection of the molecule[34] at 293 K, showing the labeling of the atoms. Full accounts of the structural information including data collection procedure and structure refinement results are provided as Supporting Information (Tables S1−S6).

EPR Measurements. The EPR experiments at 9.8 GHz were performed with a Bruker ER-200, using a 12 in. rotating magnet at fixed temperatures (298 and 80 K), and as a function of *T* between these values, with a home-built cylindrical cavity with 100 kHz field modulation.[35] The temperature was controlled and measured with a precision of 0.5° using a platinum thermometer. To orient the single-crystal samples, they were glued to a holder made of rexolite considering the crystallographic data, which defines a set x **(**$\equiv a^*$**),** y **(**$\equiv b$**),** z **(**$\equiv c$**)** of orthogonal axes (see Figure 2). This procedure allows rotating the magnetic field in the planes a^*b, ac and bc, with an uncertainty smaller than 2°. EPR spectra at 298 and 80 K were collected digitally for magnetic field orientations at 5° intervals in these three planes. One sample was mounted in a way that allowed measuring spectra with the magnetic field **B** in the (110) plane.

The spectra showed the characteristic four-line hyperfine structure due to the $I = {}^3/_2$ spin of the copper nuclei. As explained later, either one or two of these spectra were observed

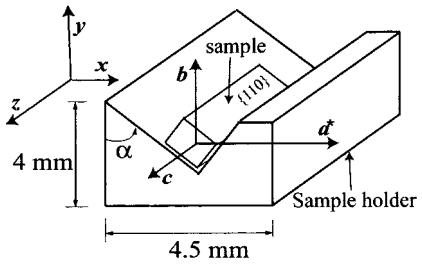

Figure 2. Sample holder used in the single-crystal EPR experiments. The angle $\alpha = 49.5°$ was calculated from the structural information in order to get the desired orientation.

depending on the field orientation and the temperature. They were simulated with a nonlinear fitting program, which assumes Gaussian line shapes for the individual resonances, where their positions and line widths are the adjustable parameters obtained from the data. EPR spectra of powdered samples were obtained at 9 and 35 GHz at *T* between 1.5 and 300 K. The measurements at 35 GHz were performed with a spectrometer described before.[36]

DSC Measurements. Differential scanning calorimetry (DSC) measurements in powder samples of Zn(D,L-histidine)$_2$ were made with a Mettler 3000 TA calorimeter from 110 to about 350 K, when the sample dehydrates. The sample was about 10 mg of freshly prepared material. The reproducibility of the data was confirmed in several runs. The calorimeter used was not calibrated, and so the data set is qualitative.

Experimental Results

Crystal Structure of Zn(D,L-histidine)$_2$. The present study improves the precision of the early structural determination of Zn(D,L-histidine)$_2$ at room temperature reported by Harding and Cole[14] in 1963, and adds new data at 150 K. The main results are similar at both *T* (see Table 1), so we emphasize only the new findings and the aspects that are relevant to our investigation. Full tables of the results at 293 and 150 K for the crystal data and structure refinement for Zn(D,L-histidine)$_2$ (Table S1), fractional atomic coordinates and equivalent isotropic parameters for all non-hydrogen atoms (Table S2), listings of atomic anisotropic thermal parameters (Table S3), hydrogen atoms positions (Table S4), bond lengths and angles (Table S5), and hydrogen bonds lengths and angles (Table S6), are included in the Supporting Information. The crystal structure consists of a packing of isolated Zn($C_6H_8N_3O_2$)$_2$ and water molecules, linked by hydrogen bonds. The Zn atom, in a special lattice position on a crystallographic 2-fold axis, is surrounded by two symmetrically related histidine ligands, bonded to the δ-nitrogen atom N(2) of the imidazole ring (Zn−N(2) bond length ≈ 2.00 Å), and to the N(1) atom of the amino group (Zn−N(1) bond length ≈ 2.05 Å) of each histidine. The geometry of the Zn center is a distorted tetrahedron (see Figure 1), with angles ranging from 95° to 122° and C_2 point symmetry. Two O(1) carboxyl oxygen atoms of each histidine at 2.89 Å from the Zn ion, suggest a weak bond interaction. The imidazole ring and the C(3) atom are nearly coplanar. The Zn atom is ∼0.19 Å out of the imidazole plane at 293 and 150 K. The carboxylate group, C(2) and N(1) atoms are also nearly coplanar. The structure contains molecules of Zn(D-histidine)$_2$ and Zn(L-histidine)$_2$ related to each other by inversion centers. Bond distances and angles obtained at 293 and 150 K (Table S5) differ in the range of the standard deviation.

There are three water molecules in the asymmetric unit of the structure. The oxygens of two of them (O(3) and O(4)) are in general positions. The other one (O(5)) is in a 2-fold axis. The largest structural differences observed between the two temperatures involve these water molecules and the hydrogen bonds present in the compound (Table S6). At 293 K, the thermal parameters of the water molecules (Table S3) are relatively large, with maximum isotropic thermal parameter for O(4). The water oxygen O(3) has an anisotropic thermal ellipsoid significantly larger than those of O(4) and O(5). The ratio between the maximum and minimum principal values of the thermal ellipsoids, R_{max}/R_{min}, are 3.62, 3.18, and 2.02 for O(3), O(4), and O(5), respectively, at 293 K. At 150 K the crystal structure refinement shows a split of the O(3) water molecule in two different positions, $O(3)_I$ and $O(3)_{II}$, each with 50% occupation, separated by 0.68 Å. At 150 K the R_{max}/R_{min} values for $O(3)_I$, $O(3)_{II}$, O(4), and O(5) are 2.01, 1.42, 3.09, and 6.30, respectively, indicating a possible disorder of the O(5) water molecule into two positions. However, no other evidence of disorder was found, and O(5) was treated as ordered. The hydrogens of the water molecules were located in the difference Fourier maps (see Table S4).

The structure of Zn(D,L-histidine)$_2$ has an intricate scheme of hydrogen bonds (Table S6). Two of them connect Zn(histidine)$_2$ molecules in the crystal lattice. The others provide links between water and Zn(histidine)$_2$ molecules, or between water molecules.

The main structural differences between 293 and 150 K are as follows:

(i) At 150 K the water oxygen O(3) is randomly disordered into two positions separated by 0.68 Å (Table S2), each having 50% occupation.

(ii) Due to the disorder of the O(3) water molecule there is a consequent split of H(10) into two positions ($H(10)_I$ and $H(10)_{II}$), reflecting a change in the H-bond network.

(iii) The positions of the water oxygens O(4) and O(5) and their bonded hydrogen (H(11), H(12), and H(13)) remain unique, but small changes in the H-bonds distances and angles appear (Table S6).

If copper ions substitute zinc ions in the lattice of Zn(D,L-histidine)$_2$, the four special sites in the unit cell (called "e" sites in ref 31) are magnetically equivalent for any orientation of the applied magnetic field **B**. In one pair of sites, the metal ions are bonded either to two D-histidine molecules, or to two L-histidine molecules. These two sites are related by an inversion operation, and they give identical EPR spectra. The second pair of sites is obtained from the first by a simple translation and, consequently, their EPR spectra are also identical.

EPR Results and Analysis

Spin Hamiltonian for Cu(II) Ions in Cu:Zn(D,L-histidine)$_2$. The spin Hamiltonian describing the energy levels of isolated Cu(II) ions relevant to the EPR measurements is

$$H_i = \mu_B \mathbf{S}_i \cdot \boldsymbol{g}_i \cdot \mathbf{B} + \mathbf{I}_i \cdot \boldsymbol{A}_i \cdot \mathbf{S}_i \qquad (1)$$

where μ_B is the Bohr magneton, $\mathbf{S}_i$ and $\mathbf{I}_i$ are the effective electronic spin ($\mathbf{S} = {}^1/_2$ for copper ions), and nuclear spin ($\mathbf{I} = {}^3/_2$ for the 63 and 65 natural copper isotopes), respectively, for Cu ions in site *i* of the structure of Zn(D,L-histidine)$_2$ ($i = 1, n$). **B** is the applied magnetic field, $\boldsymbol{g}_i$ and $\boldsymbol{A}_i$ are the *g* and copper hyperfine tensors, respectively, and *n* is the number of magnetically different sites occupied by copper ions in the lattice.

The energy levels of the spin Hamiltonian of eq 1 were calculated by Weil[37,38] up to second order of perturbations, and we used their results to analyze our experimental data. The

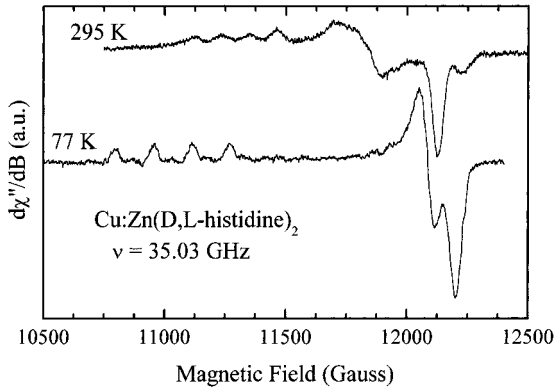

Figure 3. 35.03 GHz EPR spectra of a powder sample of Cu:Zn(D,L-histidine)$_2$ at 295 and 77 K.

magnetic field position B_{im} of the EPR line corresponding to the projection m of I_{iz} is

$$B_{im} = \frac{h\nu_0}{g_i\mu_B} - \frac{A_i}{g_i\mu_B} m + \text{second-order corrections} \quad (2)$$

where h is the Planck constant, ν_0 is the microwave frequency, $g_i^2(\theta,\phi) = \boldsymbol{h}\cdot\boldsymbol{g}_i\cdot\boldsymbol{g}_i\cdot\boldsymbol{h}$ and $g_i^2A_i^2(\theta,\phi) = \boldsymbol{h}\cdot\boldsymbol{g}_i\cdot\boldsymbol{A}_i\cdot\boldsymbol{A}_i\cdot\boldsymbol{g}_i\cdot\boldsymbol{h}$ are the projections of the tensors $\boldsymbol{g}_i$ and $\boldsymbol{g}_i\cdot\boldsymbol{A}_i$ along $\boldsymbol{h} = \mathbf{B}/|\mathbf{B}|$, the unit vector along **B**. The sign of A_i in eq 2 is irrelevant for the purpose of this work and we use $A_i > 0$ in the labeling of the hyperfine components. The positions B_{im} and the peak to peak line width ΔB_{im} of each hyperfine component (m) were obtained from simulations of the single-crystal spectra, proposing as line shapes the sum of the derivatives of four Gaussian curves with different positions and line widths. At each angle, the values of g_i^2 and $g_i^2A_i^2$ were obtained from the field positions using eq 2 considering the second-order corrections,[37] and a procedure proposed earlier.[22]

EPR Study of Powder Samples. Powder samples of Zn(D,L-histidine)$_2$ were studied at 9.4 and 35 GHz at temperatures 295, 77 and 1.5 K. Our 9 GHz data at 295 and 77 K are consistent with those obtained by Rockenbauer et al.[23] The 35 GHz spectra at 295 and 77 K are shown in Figure 3. The spectrum at 295 K reflects orthorhombic symmetry with $g_1 \neq g_2 \neq g_3$, and resolved hyperfine structure in the region of g_3. The low-field hyperfine component is broader than the high-field component. The variation of the line width with hyperfine component in the powder spectra obtained at 35 GHz is less important than that observed at 9 GHz. At 77 K the spectrum approaches axial symmetry (with $g_1 \approx g_2$), and shows an increase of g_3 and A_3 from the values at 295 K. At 1.5 K the spectra observed at both microwave frequencies display large changes with microwave power and field-sweep frequency, which are attributed to severe passage effects[39] (data not shown). Analyses of the 35 GHz powder spectra at 295 and 77 K (Figure 3) give g factors slightly different than those obtained from the single-crystal study described below, performed at 9.4 GHz. However, only single-crystal data at 35 GHz would allow confirming this point. Accurate single-crystal measurements are not allowed by our experimental setup. A deuterated powder sample was studied at 9.4 GHz. Within experimental uncertainties the results are identical to those in the nondeuterated sample.

EPR Study of Single-Crystal Samples. The $xyz \equiv a^*bc$ system of axes ($\boldsymbol{a}^* = \boldsymbol{b} \times \boldsymbol{c}$) is used in the analysis and presentation of the EPR data in single crystals. Figure 4, a and b, displays the spectra observed at X-band for the magnetic field **B** oriented along the ***b***-axis at 298 and 80 K, respectively. At

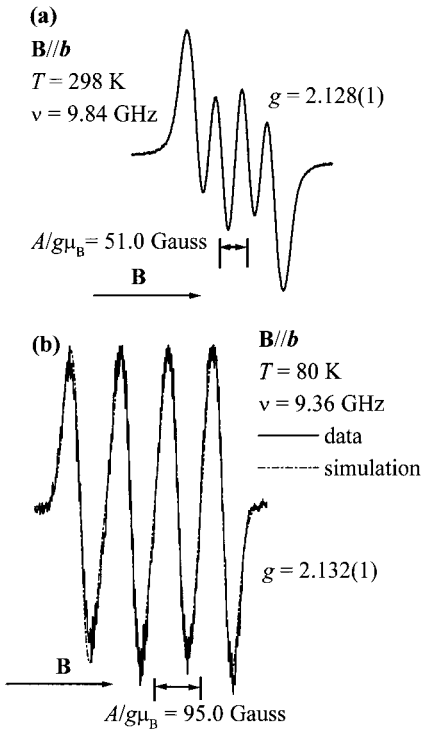

Figure 4. EPR spectra observed at 298 K (a) and 80 K (b) for the magnetic field along the ***b***-axis. Simulations with the sum of four derivatives of Gaussian curves, where the positions and line widths were taken as adjustable parameters, are included.

both temperatures (T) one observes one group of four hyperfine components, as expected for the $I = {}^3/_2$ nuclear spins of the two copper isotopes, which have similar magnetic moments. At 298 K (Figure 4a), $g = 2.128(1)$ and $A/g\mu_B = 51.0(5)$ G, and the line widths of the four hyperfine components are not equal. At 80 K g changes to 2.132(1) and $A/g\mu_B$ to 95.0(5) G (Figure 4b), while the line widths of the hyperfine components are equal. Spectra like those in Figure 4a,b (one EPR-distinguishable copper site) also occur for the magnetic field **B** in the *ac* crystal plane, at any temperature.

Figure 5, a and b, displays the spectra observed for **B** along the direction $\theta = 120°$, $\phi = 90°$ in the *bc* plane, at $T = 298$ and at 80 K, respectively. The spectra observed at 298 K (circles in Figure 5a) display a single group of four hyperfine components, having line widths that depend strongly on the nuclear spin quantum number m. The solid line on top of the circles in Figure 5a displays the simulation of the spectra assuming Gaussian line shapes with different line widths for the four hyperfine components. To stress the large differences between the line widths of the hyperfine components we include the simulated individual components as dotted lines in Figure 5a. The spectrum observed at 80 K (see Figure 5b) can be decomposed as the sum of two hyperfine groups (I and II), each with 50% population,[40] having four hyperfine components with similar line widths. The simulation of the observed spectrum is included in Figure 5b, as well as the contributions of the individual groups I and II of hyperfine components. For all magnetic field orientations different from the ***b***-axis, and out of the *ac* plane, at 298 and at 80 K, the EPR spectra are similar to those shown in Figure 5a (at 298 K) and Figure 5b (80 K). The spectra at 298 K (Figure 5a) indicate that all copper ions are in magnetically equivalent sites ($n = 1$ in eq 1). As explained before, this result is expected from the crystallographic data if copper ions replace zinc ions in their special sites of the unit cell. However, the strong variation of the line width with the

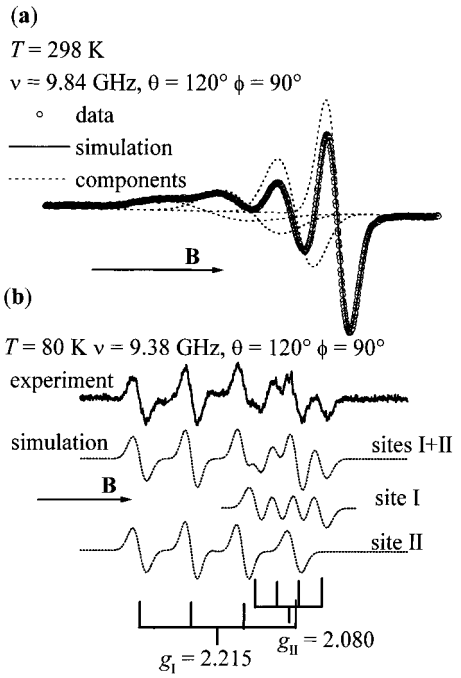

Figure 5. EPR spectra observed at 298 K (a), and 80 K (b), for the magnetic field along the direction $\theta = 90°$, $\phi = 120°$ in the *ab* plane. Simulations of the experimental results with the sum of four derivatives of Gaussian curves are included.

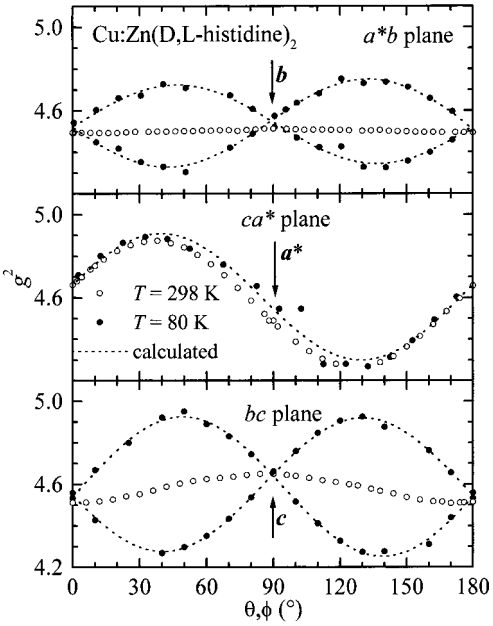

Figure 6. Angular variation of the g^2 factor in the three crystallographic planes, as obtained from the data at 298 K and at 80 K. There is one set of values of g^2 at 298 K (one set of copper ions), but two at 80 K (two sets of copper ions).

hyperfine component observed at 298 K is an unexpected experimental result. The spectra at 80 K shows two distinguishable sites for copper ions. Thus, at 80 K, the point symmetry of the copper sites is lower than that expected from the space symmetry of Zn(D,L-histidine)$_2$ when Cu ions replace Zn ions.

The *g* factor, hyperfine coupling parameter *A*, and line widths ΔB_m of the resonances were obtained at each magnetic field orientation as explained before. Figures 6 and 7 display the angular variations of g^2 and g^2A^2 in the planes *a***b*, *ac*, and *bc*, at 298 K (one copper site, empty circles) and 80 K (two copper sites, filled circles). The line widths ΔB_m measured in the same

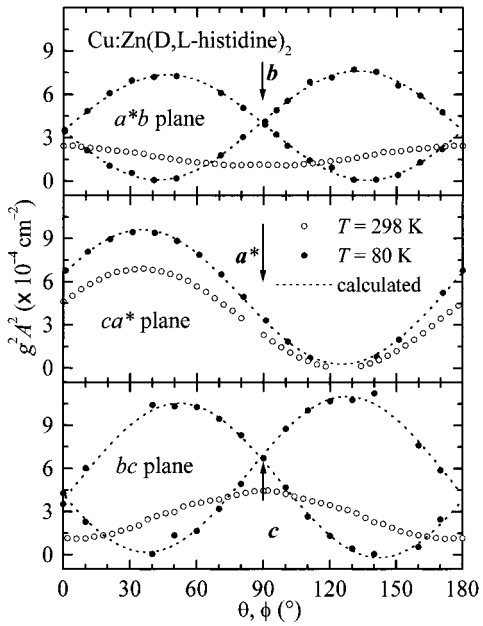

Figure 7. Angular variation of $g^2A^2(\theta,\phi)$ in the three crystallographic planes obtained from the data at 298 and at 80 K. There is one set of values of g^2A^2 at 298 K (one set of copper ions) but two at 80 K (two sets of copper ions).

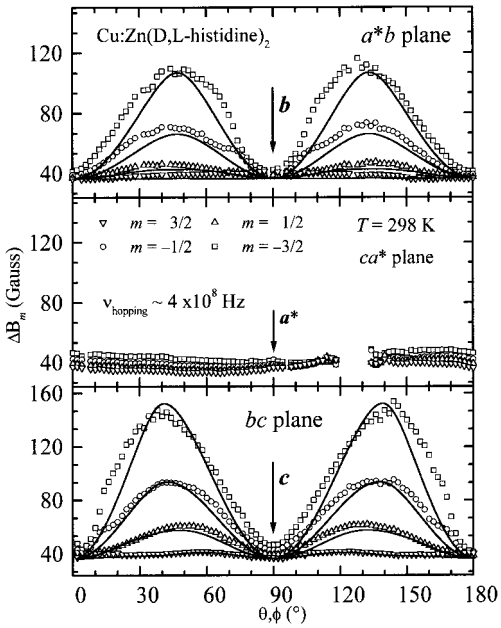

Figure 8. Angular variation of the peak-to-peak line width of the different hyperfine components of the spectra observed in the planes *a***b*, *ac*, and *bc*. Solid lines are obtained from the model leading to eq 7 with $\nu_h = 0.8 \times 10^9$ 1/s.

planes at 298 K for each hyperfine component are displayed in Figure 8 as a function of angle. The line width data at 80 K do not show special features, and are not shown. The EPR spectra were also studied at 298 K with the magnetic field in the (110) plane (data not shown).

The angular variations of g^2, g^2A^2, and the line width displayed in Figures 6, 7, and 8 show that the monoclinic ***b***-axis is a binary C_2 axis relating the two different Cu(II) spectra observed at 80 K. The spectra of each individual copper, however, do not have C_2 point symmetry around ***b*** in this *T* range. The angular variations of the spectrum observed at 298 K have the full C_2 symmetry of the Zn sites. The hyperfine interaction of the Cu(II) ions with the spins $I(^{14}N) = 1$ of the

TABLE 2: (a) Eigenvalues and Eigenvectors of the Tensors *g* and *A* Measured at 298 K in Cu:Zn(D,L-histidine)$_2$. (b) Eigenvalues and Eigenvectors for the Tensors g_I, g_{II}, A_I and A_{II} at 80 K

		eigenvectors		
eigenvalues		x = *a**	*y* = *b*	*z* = *c*
(a) Eigenvalues and Eigenvectors of the Tensors ***g*** and ***A***				
g tensor (298 K)				
$g_1 = 2.071(1)$	ξ	0.721	−0.025	−0.692
$g_2 = 2.124(1)$	η	0.002	0.999	0.033
$g_3 = 2.204(1)$	ζ	0.692	−0.022	0.721
A tensor **(**298 K**)**				
$A_1 = 25(1) \times 10^{-4}$	ξ	0.72	−0.02	−0.69
$A_2 = 48(1) \times 10^{-4}$	η	0.01	0.99	0.03
$A_3 = 120(1) \times 10^{-4}$	ζ	0.69	−0.01	0.72
(b) Eigenvalues and Eigenvectors for the Tensors g_I, g_{II}, A_I, and A_{II}				
g tensors (80 K)				
$g_1 = 2.057(1)$	ξ_I,ξ_{II}	±0.558	−0.365	∓0.745
$g_2 = 2.081(1)$	η_I,η_{II}	±0.642	0.759	±0.109
$g_3 = 2.269(1)$	ζ_I,ζ_{II}	±0.526	−0.539	±0.667
A tensors (80 K)				
$A_1 = 0(1) \times 10^{-4}$	ξ_I,ξ_{II}	±0.41	−0.53	∓0.74
$A_2 = 37(1) \times 10^{-4}$	η_I,η_{II}	±0.75	0.66	±0.06
$A_3 = 167(1) \times 10^{-4}$	ζ_I,ζ_{II}	±0.52	−0.53	±0.67

[a] The eigenvectors of g_I and g_{II}, and of A_I and A_{II} differ in the sign of one components. The eigenvectors are referred to the coordinate system defined by *xyz* = *a***bc*. Hyperfine couplings are in cm^{-1}.

two nonequivalent nitrogen ligands is not resolved in the spectra observed for any orientation of the applied magnetic field. This should be a consequence of the high multiplicity of this structure in the case of four $I_N = 1$ nitrogen ligands (up to 81 components).

The components of the tensors g^2 and g^2A^2 were evaluated from the data in Figures 6 and 7 by the least-squares method. They were used to obtain the components of ***g*** and ***A***, assuming that they are symmetric tensors.[22] The eigenvalues and eigenvectors of ***g*** and ***A*** calculated from the data at 298 K are given in Table 2a. At 80 K there are four ways to assign the two groups of resonances observed in the three studied planes. Each one was analyzed and the corresponding g^2 and g^2A^2 tensors were calculated. Two sets, having the same eigenvalues and eigenvectors and related by a C_2 rotation around ***b***, are the valid solution and reproduce the powder spectrum and the single-crystal data in the plane (110). The other two are invalid solutions that do not reproduce the powder data and the data in the (110) plane. They are a consequence of a wrong assignment of the resonances in the three planes. Eigenvalues and eigenvectors of the g_I, g_{II}, A_I, and A_{II} tensors calculated from the data at 80 K are given in Table 2b, where double signs indicate differences between some components of the eigenvectors of g_I and g_{II}, and of A_I and A_{II}.

The orientations of the eigenvectors of the ***g*** tensor within the Zn(D,L-histidine)$_2$ molecule at 80 and 298 K are shown in Figure 9, a and b, respectively, in projections along the ***b***-axis. The eigenvectors ζ_I and ζ_{II} corresponding to the axial directions (related to g_3) of the *g* tensors of spectra I and II at 80 K are shown in Figure 9a. The angle between ζ_I or ζ_{II} and the directions connecting the Zn ion with one of the amino nitrogen (N(1)) neighbors for each particular state is ∼8°. The other two eigenvectors of ***g*** are approximately in the plane containing the two imidazole nitrogens N(2), and the other amino nitrogen. Figure 9b displays the directions ξ, η, and ζ corresponding to the eigenvalues g_1, g_2 and g_3 (see Table 2a), respectively, of the orthorhombic ***g*** tensor observed at 298 K.

We also measured the temperature dependence between 80 and 300 K of the *g* factor, hyperfine coupling and line width,

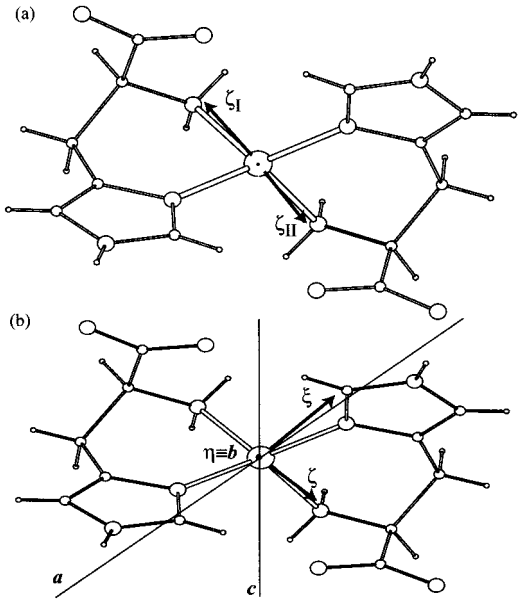

Figure 9. (a) Orientation of the axial directions ζ_I and ζ_{II} of the ***g*** tensors of the two copper sites observed at 80 K. (b) The three principal directions ξ, η, and ζ of the ***g*** tensor of the single copper site observed at 298 K.

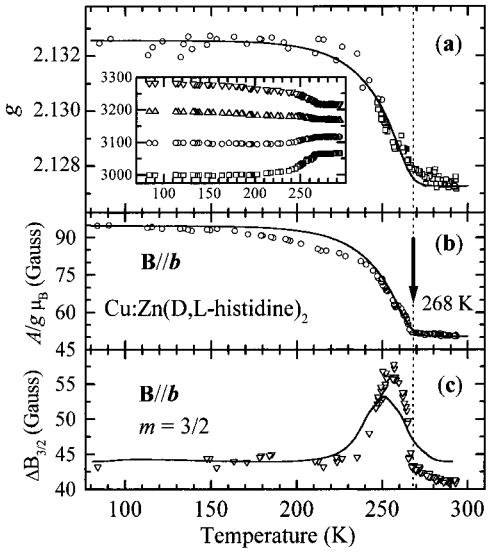

Figure 10. Temperature dependence of (a) the *g* factor, (b) the Cu(II) hyperfine coupling parameter, and (c) the observed peak to peak line width of the resonance $m = 3/2$, for **B**||***b***. The dashed vertical line indicates the transition temperature $T_c = 268$ K. The inset of part (a) shows the observed temperature variation of the positions of the resonances from which the values of *g* and *A* were calculated. The solid lines in (a), (b), and (c) are obtained with the four-states model.

for the orientations of the magnetic field of Figures 4 and 5. The results obtained for **B** along the ***b***-axis are shown in Figure 10. The observed temperature variation of the positions of the resonances is shown in the inset of Figure 10a. From these values we calculated the *g* factor (Figure 10a) and the hyperfine parameter (Figure 10b), which show an abrupt change at $T_c = 268$ K. Above this temperature they remain constant. The line width of the $m = {}^3/_2$ transition (Figure 10c) displays a peak value around 254 K. The line width of the $m = -{}^3/_2$ transition (data not shown) displays a peak at the same temperature, and is about 10% narrower in the region close to the peak. Figure 11 displays the evolution of the two groups of resonances observed at temperatures below $T_c = 268$ K, to the regime of

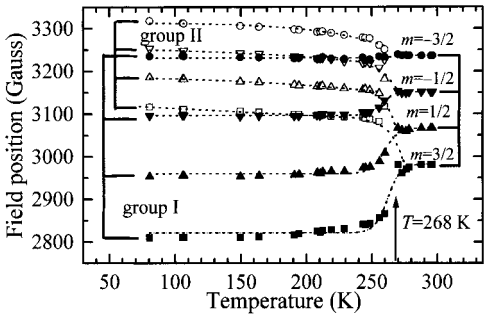

Figure 11. Temperature dependence of the magnetic field positions of the resonances from groups I and II along the direction $\theta = 90°$, $\phi = 120°$. The collapse of these two groups into one group at T_c is depicted by lines, which are included as an aid to the eye.

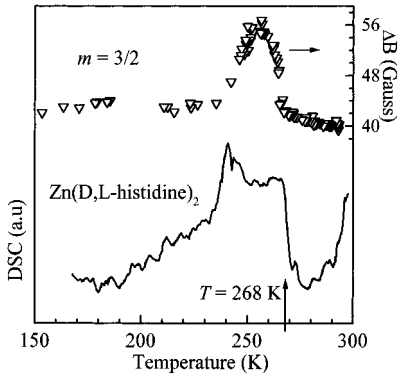

Figure 12. Differential scanning calorimetry results for pure Zn(D,L-histidine)$_2$ as a function of temperature (lower curve). For comparison we show in the upper curve the line width ΔB_m for the $m = {}^3/_2$ transition, in the same temperature range.

one group of resonances, above T_c, for the magnetic field applied along $\theta = 120°$ and $\phi = 90°$ in the *bc* plane (as in Figure 5). Positions, *g* factor and hyperfine coupling, display a transition at the temperature T_c. The line width is nearly constant in the studied *T* range, except around a peak between 240 and 268 K. There is a residual contribution of about 36 G, common to all hyperfine components, plus a contribution dependent on *m*, which peaks about 20 G for the low-field hyperfine transition around 258 K. We have not observed hysteresis effects in the EPR measurements as a function of temperature. This may be due to the slow temperature variation rate used in our experiments (~8°/h), and indicates that no structural damage is produced in the sample during the experiments, and also that any other process in the sample is much faster than that speed.

Calorimetric Results

The results of the DSC measurements in pure Zn(D,L-histidine)$_2$ are displayed in Figure 12 showing **a** wide peak spreading between 230 and 270 K. In order to emphasize the similar position and spread of the peaks, we include in Figure 12 the temperature variation of the line width of the $m = {}^3/_2$ transition for **B** along the ***b***-axis.

Summary of the Experimental Results

(i) The crystal structures observed at 293 and 150 K in Zn(D,L-histidine)$_2$ are the same, with minor changes in the lattice parameters. Changes occur for a water molecule that shows structural disorder. At 293 K, the water oxygen O(3) shows a large thermal anisotropy. At 150 K this anisotropy evolves to a situation where O(3) occupies two possible lattice sites with equal probability.

(ii) EPR spectra of powder samples at 9.4 and 35 GHz display large changes at temperatures around 268 K. At 9.4 GHz, and above this temperature, the line widths of the low-field peaks depend strongly on the hyperfine components. This dependence is weaker at 35 GHz.

(iii) At 80 K (Figure 5b) the single-crystal spectra are attributed to two equally populated types of Cu(II) having approximately axial symmetry (see Table 2a), with equal populations, and related each other by a C_2 symmetry operation around ***b***. The axial directions of the ***g*** and ***A*** tensors for each site are close to the direction defined by the Zn site and one of the amino N(1) nitrogens in the pure crystal.

(iv) When increasing the temperature, and around $T_c = 268$ K, the two Cu(II) spectra merge to a single one with a ***g*** tensor that is approximately the average of the ***g*** tensors corresponding to the two sites at lower *T* (see Tables 2a,b). The hyperfine coupling tensor at 298 K greatly deviates from the average of the tensors at 80 K. The single-crystal EPR spectra observed at 298 K can be assigned to one copper site. The ***g*** and ***A*** tensors have rhombic symmetry. These spectra display a strong variation of the line width with the hyperfine component *m*, except for **B** along the ***b***-axis or in the *ac* plane.

(v) Cooling from 268 to 240 K, we observe a large increase of the hyperfine coupling parameter (Figures 10 and 11). The resonances shift and broaden. Below 240 K the variations of the spectra with *T* are small. The line width displays a peak value around 254 K (Figure 10c).

(vi) The specific heat C_d shows an anomaly between 230 and 270 K, the same temperature range as for the peak value of the line width (compare in Figure 12 the temperature dependences of C_d and the line width).

These experimental findings are addressed and explained in the following sections

Theoretical Section

To explain the EPR data we propose that the copper ions and their ligands do not stay fixed in time in the special positions of the lattice attributed to the zinc ions, but hop randomly between different states or environments. The X-ray data suggest that the result at 293 K corresponds to structural disorder with a fast dynamics. When the temperature is lowered, the position of O(3) is randomly frozen into one of the two possible sites. Other water molecules may display similar but weaker effects. From the point of view of EPR, when the dynamics of the states is slow compared with times characteristic of the experiment we observe the sum of the individual spectra. When it is fast, the individual spectra merge to a single average spectrum. The dynamics of the copper environment and its effect on the magnetic resonance spectra are analyzed within Anderson's theory,[41] which is summarized below.

In a first approximation, and considering our EPR data at 80 K, we assume that the copper ions may be in one of two states, in positions different from those of the Zinc site in Zn(D,L-histidine)$_2$ without C_2 point symmetry, and related to each other by a C_2 operation around the ***b***-axis. This assumption explains the main experimental findings, but has to be extended to a more detailed four-states model in order to explain the data obtained along any magnetic field orientation, the changes with *T* of the hyperfine coupling, and the peak of the line width around 254 K. This four-states model considers explicitly the role of the Jahn−Teller distortions and is supported by the X-rays and specific heat data.

Anderson's Theory for Motional Narrowing and Collapse. Anderson[41] introduced a theory that considers the effects of

molecular movements in magnetic resonance spectra. The spin variables are treated quantum mechanically, while the spatial displacements are treated as classical variables. The typical effects on the EPR spectra of random molecular hopping between equilibrium situations are narrowing, changes in the line shape, and collapse of the resonances. From these spectral changes it is possible to obtain information about the molecular movements, as hopping rates and activation energies. Anderson's theory has been also used to study the dynamics of molecular groups that show rotational tunneling,[42] dynamical Jahn−Teller effect,[43,44] or spin-flip processes.[45]

According to Anderson's theory,[41] when the frequency of a spin system changes randomly between particular molecular states, the line shape $I(\omega)$ of the resonance turns out to be the Fourier transform of a correlation function $\phi(\tau)$, related to the molecular dynamics:

$$I(\omega) \propto \int \exp(-i\omega\tau)\, \phi(\tau)\, d\tau \qquad (3)$$

In the absence of saturation, $\phi(\tau)$ becomes[41]

$$\phi(\tau) = \mathbf{W} \exp[\tau(i\Omega + \Pi)]\cdot\mathbf{1} \qquad (4)$$

The components W_i of the vector $\mathbf{W}$ in eq 4 give the population of the accessible states. $\mathbf{1}$ is a vector with all components equal to unity, and Ω is a diagonal matrix whose elements ω_i are the absorption frequencies in the absence of dynamics. The matrix Π has elements $\Pi_{jk} = p_{jk}$ and $\Pi_{jj} = -\Sigma_{j\neq k}\, p_{jk}$, where p_{jk} is the transition rate between the accessible states j and k. Anderson[41] and Sack[46] solved eq 3 considering eq 4, and obtained for the line-shape function:

$$I(\omega) \propto \mathrm{Re}\{\mathbf{W}\cdot(i\omega\mathbf{E} - i\Omega + \Pi)^{-1}\cdot\mathbf{1}\} \qquad (5)$$

where $\omega\mathbf{E}$ is the unit matrix $\mathbf{E}$ times the constant ω. Equation 5 is used below in the analysis of the EPR data in terms of dynamical models (see refs 34 and 35 for more details on Anderson's theory). For Cu ions with nuclear spin $^3/_2$ ($m = {}^3/_2$, $^1/_2$, $-{}^1/_2$, $-{}^3/_2$), we assume that hopping transitions occur only between states with the same m, and the rate ν_h is independent of m.[49] The transition rate p_{jk} is taken as the product $W_j\nu_h$ between the population W_j of the departing state j and a hopping rate ν_h, related to the transition probability.[46]

Two-States Model. In this model (described in Figure 13a−c) we propose that the copper ions in Zn(D,L-histidine)$_2$ may be in states I or II defined by EPR spectra having the $\boldsymbol{g}$ tensors $\boldsymbol{g}_I$ and $\boldsymbol{g}_{II}$ and hyperfine coupling tensors $\boldsymbol{A}_I$ and $\boldsymbol{A}_{II}$, measured at 80 K (see Table 2). $\boldsymbol{g}_{II}$ and $\boldsymbol{A}_{II}$ are obtained from $\boldsymbol{g}_I$ and $\boldsymbol{A}_I$ by a C_2 symmetry operation. In the absence of dynamics the resonance fields B_{im} can be calculated with the spin Hamiltonian of eq 1 and the peak-to-peak line widths ΔB_{im} (i = I, II; $m = \pm{}^1/_2, \pm {}^3/_2$) are equal to a residual width ΔB_0. Figure 13a sketches the geometry of states I and II suggested by the EPR data at 80 K. They have approximate axial symmetry around the directions connecting the Zn (Cu) site with the amine nitrogens N(1).

The magnetic field splitting between resonances with the same m corresponding to the states I and II is

$$\delta B_m(\theta,\phi) = B_{Im}(\theta,\phi) - B_{IIm}(\theta,\phi) \qquad (6)$$

The energies and the equilibrium populations of the states I and II are the same ($W_{Im} = W_{IIm} = {}^1/_2$). Thus, the rates I → II and II → I are $p = \nu_h/2$. In order to hop between states the molecules have to overcome a potential barrier with activation energy ΔE^* indicated in the two-well potential of Figure 13a.

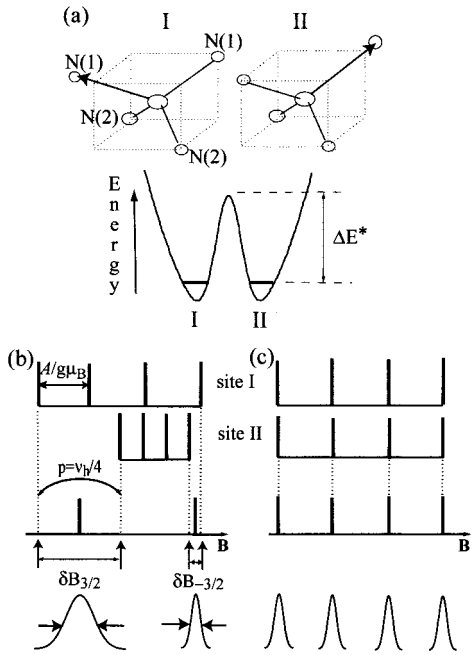

Figure 13. Two-states model. (a) Possible molecular distortions, as suggested by the data at 80 K, and potential energy curve for states I and II. (b) Narrowing and collapse of the resonances corresponding to states I and II when the g factor and the hyperfine coupling of state I are different from those of state II. For simplicity, only the resonances with $m = {}^3/_2$ and $m = -{}^3/_2$ are shown. (c) Case where the sites have the same g factor and hyperfine coupling.

The resonances corresponding to states I and II collapse into a single resonance, as a consequence of the hopping rate ν_h, in the absence of a hyperfine splitting. We consider the case when states I and II have different $\boldsymbol{g}$ and $\boldsymbol{A}$ (general magnetic field direction) in Figure 13b, and the case when the two states have equal $\boldsymbol{g}$ and $\boldsymbol{A}$ ($\mathbf{B}\|\boldsymbol{b}$ or $\mathbf{B}$ in the ac plane) in Figure 13c. When $\nu_h \ll g\mu_B\delta B_m/h$, and for $\boldsymbol{g}_I \neq \boldsymbol{g}_{II}$, $\boldsymbol{A}_I \neq \boldsymbol{A}_{II}$, the spectra display two groups of four resonances, each having the (residual) line width ΔB_0 (Figure 13b). This is the case observed below T_c, when the experiments provide information about the individual states. When $\nu_h \gg g\mu_B\delta B_m/h$, each pair of resonances with equal m collapses to the mean field $^1/_2(B_{Im} + B_{IIm})$. This collapse occurs for $\nu_h \approx g\mu_B\delta B_m/h$, when information about the states I and II is lost. According to Anderson's theory,[41] the line widths of the collapsed resonances depend on the splitting δB_m before the collapse, the hop frequency ν_h between states with equal m, and on the residual line width ΔB_0. The 8 × 8 matrix [$i\omega\mathbf{E} - i\Omega + \Pi$] (eq 5) is made of four separate 2 × 2 blocks, each corresponding to one of the four values of m. When $\nu_h > g\mu_B\delta B_m/h$, it is obtained from each of these blocks for the line width measured in field units between peaks of the derivative signal:

$$\Delta B_m(\theta,\phi) = \Delta B_0 + \frac{\sqrt{3}g(\theta,\phi)\mu_B}{8h\nu_h}\,\delta B_m(\theta,\phi)^2 \qquad (7)$$

This result is described in the lower part of Figure 13b, which shows that the resonance with $m = {}^3/_2$ is wider than that with $m = -{}^3/_2$ because $\delta B_{3/2} > \delta B_{-3/2}$. If states I and II give the same spectra (Figure 13c), it is $\delta B_m = 0$ according to the two-states model and no contributions to the line width arise from the molecular dynamics of the system.

The rate ν_h varies with T, but not with the magnetic field direction $\boldsymbol{h}$. However, a change of $\boldsymbol{h}$ changes $\delta B_m(\theta,\phi)$ (see eq 6) and thus, the contribution to the line width of eq 7 is

anisotropic. Figure 8 shows as solid lines the best fit of eq 7 to the line width data in the three planes at 298 K, obtained with $\nu_h \approx 0.8 \times 10^9\ s^{-1}$. The height of the barrier ΔE^* (defined in Figure 13a) may be estimated proposing for ν_h an activated process. Assuming that the tunneling splitting between the energies of states I and II is smaller than the barrier height ΔE^*, we use the prediction of transition state theory:[10,50−52]

$$\nu_h \approx (k_B T/h)\,[\exp(-\Delta E^*/k_B T)] \qquad (8)$$

with $T = T_c$, to obtain from ν_h an activation energy $\Delta E^* \approx 1600\ cm^{-1}$. The change of ν_h with temperature (eq 8) produces at T_c the collapse of the resonances (Figure 11).

The two-states model explains the following experimental observations:

(i) At a temperature T_c the two copper spectra observed at low T collapse to a single copper spectrum (see Figures 11). The ***g***-tensor of the collapsed spectrum is approximately the average of the ***g***-tensors of the individual sites.

(ii) Above T_c the line widths of the collapsed resonances are different for different hyperfine components for general magnetic field orientations. These line widths display a dependence on m which follows eq 7 (see solid lines in Figure.8).

However, the two states model does not explain the following features of the EPR spectra:

(i) There are changes on the positions and line widths of the resonances for a magnetic field applied along the ***b***-axis or in the *ac* plane, where the two copper sites are magnetically equivalent (Figures 4 and 10).

(ii) The splittings and line widths of the four hyperfine components observed at 298 K for **B**||***b*** are not equal (Figure 4).

(iii) The hyperfine splitting tensor ***A*** for the collapsed line differs from the average of $\boldsymbol{A}_I$ and $\boldsymbol{A}_{II}$ (Figure 7).

(iv) Even for **B**||***b*** the temperature variation of the line width displays a peak slightly below T_c (Figure 10c), in the same temperature range as the peak of the specific heat.

To explain these observations we require the more detailed model described below.

Four-States Model. In the four-states model (Figure 14) we propose that the N(1) amine nitrogen ligands[53] to the copper ions, which in the undistorted structure are related by a C_2 operation around ***b***, can move independently between two conformations, called f (far) and c (close). This gives rise to four possible states (sketched in Figure 14a). In state I the ligands are in conformations f and c. In state II they are in conformations c and f. States I and II are those considered in the two-states model; they do not have C_2 symmetry, and their ***g*** and ***A*** tensors (and the angular dependence of the EPR spectra) are related by a C_2 operation around ***b***. As in the Jahn−Teller theorem,[54] they are expected to have an energy smaller than the undistorted state. We also consider new states III and IV, with their N(1) ligands in conformations (f,f) and (c,c), respectively, with an energy splitting δE (Figure 14a). We assume that they have equal ***g*** and ***A*** tensors and give rise to the same EPR spectra. In principle, the states III and IV may have different ***g*** and ***A*** tensors, but we do not have enough experimental information to evaluate their difference, but only the average values. At low T only states I and II are populated. The populations of states III and IV increase when T is increased, at the expense of states I and II. Considering the nuclear spin state m, each state may be labeled as (i,m), where i = I, II, III, and IV, and $m = \pm 1/2, \pm 3/2$. Figure 14a describes with arrows the possible hopping transitions between the states. A transition from state I (f,c) to states III (f,f) or IV (c,c), or from state II (c,f) to states III and IV is a hop from conformation f to c (or c to f) of one of the ligands (see Figure 14a). Transitions from I to II or from III to IV require a hop of both ligands, and they are not considered. As in the two-states model, the dynamics of the system is described by a hopping rate ν_h, and the transition probabilities p_{jk} are products of the population of the states, times the hopping rate. We also assume that hopping transitions do not change the nuclear spin state m. The EPR spectra of the system are defined by the tensors ***g*** and ***A*** of each state, the hopping rate ν_h, and the populations $W_I = W_{II}$ and $W_{III} = W_{IV}$. These populations would be related to a Boltzmann factor if they were simply related to the energy of each state. However, the results of the X-rays study, and the specific heat and line-width data in Figure 12, point to a cooperative process. In pure Zn(D,L-histidine)$_2$ the dynamical disorder of a water molecule in two positions, observed with X-rays at 293 K, is frozen in as static disorder at low temperature. In the Cu-doped sample and in the same T range (Figure 12) anomalies in the EPR spectra are observed. Thus, the dynamical disorder of the ligands to a copper ion may be different than the disorder of the waters in the pure lattice, but the dynamics follows approximately equal temperature dependences. The populations of states I, ..., IV are assumed to be

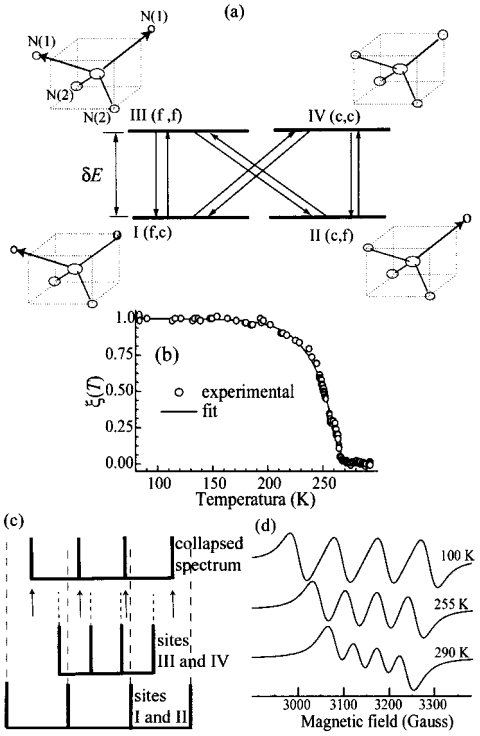

Figure 14. Four-states model. (a) Description of the four-states energy level scheme and hopping transitions between the states. (b) Variation with T of the order parameter $\xi(T)$ experimental values and fit with eq 12 with parameters given in the text. (c) Bar diagram of the EPR lines corresponding to sites I and II, to sites III and IV, and of the collapsed resonances at high temperature, for **B**||***b***. (d) Spectra calculated for **B**||***b*** at different temperatures using the four-states model.

$$W_I = W_{II} = {}^1/_4(1 + \xi(T)) \quad W_{III} = W_{IV} = {}^1/_4(1 - \xi(T)) \qquad (9)$$

In eqs 9 $\xi(T)$ is the order parameter that follows the lattice disorder. Above T_c, $\xi = 0$ and $W_i = 1/4$ for i = I, ..., IV. At low T, $\xi = 1$, and $W_I = W_{II} = 1/2$ (as in the two-states model) and $W_{III} = W_{IV} = 0$.

The hyperfine parameter $A_h(T)$ measured for **B** along ***h*** = **B**/|**B**| in the collapsed regime is

$$A_h(T) = W_I A_{Ih} + W_{II} A_{IIh} + W_{III} A_{IIIh} + W_{IV} A_{IVh} = {}^1/_4(A_{Ih} + A_{IIh} + A_{IIIh} + A_{IVh}) + {}^1/_4(A_{Ih} + A_{IIh} - A_{IIIh} - A_{IVh})\xi(T) \quad (10)$$

where A_{ih} is the hyperfine splitting for site i, and we used eq 9. A similar equation may be written for $g_h(T)$. The hyperfine splittings A_{Ih} and A_{IIh} are measured at 80 K. The values of $A_{IIIh} = A_{IVh}$ are calculated for each field orientation from the data at 80 and 298 K. When $\xi = 0$ (298 K) the observed splitting is

$$A_h = {}^1/_4(A_{Ih} + A_{IIh} + A_{IIIh} + A_{IVh})$$

and thus

$$A_{IIIh} = A_{IVh} = 2A_h - {}^1/_2(A_{Ih} + A_{IIh}) \quad (11)$$

In the case when $\boldsymbol{A}_{III} \neq \boldsymbol{A}_{IV}$, the right side term should be equal to ${}^1/_2(A_{IIIh} + A_{IVh})$. A fit of the angular variation of $A_{IIIh}(\theta,\phi)$ calculated with eq 11 with a tensorial function allowed to calculate the components of $\boldsymbol{A}_{III}$ and $\boldsymbol{A}_{IV}$. A similar procedure allowed us to calculate the components of $\boldsymbol{g}_{III}$ and $\boldsymbol{g}_{IV}$. These values are given in Table 3.

We calculated $\xi(T)$ from the observed temperature dependence of the position of the low field resonances for $\mathbf{B}\|\boldsymbol{b}$, shown in the inset of Figure 10a. Similar results may be obtained from the data on $A_h(T)$ or $g_h(T)$ in Figure 10, a and b. The values of $\xi(T)$, shown in Figure 14b, are well fitted by the function

$$\xi(T) = 1 - \left\{1 + \exp\left[-\frac{T - \sigma \ln(2^{1/\gamma} - 1) - T_0}{\sigma}\right]\right\}^{-\gamma} \quad (12)$$

with $T_0 = 251.1 \pm 0.2$ K, $\sigma = 2.9 \pm 0.3$ K, and $\gamma = 0.14 \pm 0.02$. Equation 12 is a modified sigmoidal function of T which holds $\xi(T) = {}^1/_2$ for $T = T_0$. The solid line in Figure 14b displays the values of $\xi(T)$ obtained with eq 12 and these parameters.

The EPR spectra of the system at a temperature T were calculated in terms of ν_h, $\xi(T)$, and the tensors $\boldsymbol{g}$ and $\boldsymbol{A}$ of the different states using Anderson's model (eq 5). The 16×16 dynamical matrix arising from the states (i,m) divides in four separate 4×4 submatrices, one for each value of m, which are diagonalized numerically at each temperature. For ν_h we assume an activated process as in the two-states model (eq 8). A value $\Delta E^* = 1000 \pm 100$ cm^{-1} ($W_I \nu_h = 6.3 \times 10^9$ s^{-1} for $W_i = {}^1/_4$) at $T = 268$ K for the activation energy was obtained from a fit of the observed spectra with the four-states model. These values should be more realistic than those calculated with the two-states model. The solid lines in Figure 10 show the change with temperature of the $\boldsymbol{g}$ factor, hyperfine splitting, and line width calculated for the magnetic field direction along the $\boldsymbol{b}$ axis with the four-states model. They reproduce fairly well the experimental results. The peak in the line width appears at a temperature slightly below T_c, and coincident with T_0 of eq 12. The model also reproduces well the small differences in the line widths of the transitions with different m, and the unequal spacing of the resonances for $\mathbf{B}\|\boldsymbol{b}$. We show in Figure 14c that these differences arise from the different values of the $\boldsymbol{g}$ factor along $\boldsymbol{b}$ of sites I and III. The dashed lines in this figure are drawn to show the different spacing between the resonances corresponding to the same m for the different sites, which produce a variation of the line width with m. Spectra calculated for $\mathbf{B}\|\boldsymbol{b}$ at three temperatures using the four-states model and Anderson's formalism (Figure 14d) are in good agreement with the measured spectra.

TABLE 3: Eigenvalues and Eigenvectors of the Tensors $\boldsymbol{g}_{III} = \boldsymbol{g}_{IV}$ and $\boldsymbol{A}_{III} = \boldsymbol{A}_{IV}$ Obtained Using the Four-States Model (Eq 11)

		eigenvectors		
eigenvalues		x = a^*	$y = b$	$z = c$
$\boldsymbol{g}$ tensor (298 K)				
$g_1 = 2.081(2)$	ξ	0.744	−0.003	−0.668
$g_2 = 2.115(2)$	η	0.007	0.999	−0.035
$g_3 = 2.194(2)$	ζ	0.744	−0.003	0.668
A tensor (298 K)				
$A_1 = 30(3) \times 10^{-4}$	ξ	0.632	−0.06	−0.77
$A_2 = 0(3) \times 10^{-4}$	η	0.03	0.99	−0.05
$A_3 = 92(3) \times 10^{-4}$	ζ	0.77	0.009	0.63

[a] The eigenvectors are referred to the coordinate system defined by $xyz = a^*bc$. Hyperfine couplings are in cm^{-1}.

Discussion

The EPR data in Zn(D,L-histidine)$_2$ of Rockenbauer et al.[23] had the typical limitations of the powder spectra: it is not possible to identify the number of Cu(II) spectra, and the information about the copper sites cannot be related to specific directions in the crystal. However, these authors were able to detect anomalies on the spectra below room temperature. The single-crystal EPR study reported here provides a detailed view of the electronic properties of the dopant copper ions. Besides, the X-ray and DSC studies in the pure compound give important information about the host lattice that has been related to the EPR data. In the EPR experiments reported here we have not observed hysteresis effects, as reported by Rockenbauer et al.[23] Also, we observed that the transition at 268 K is already in pure samples of Zn(D,L-histidine)$_2$, i.e., in the absence of copper doping.

Our experimental results reflect properties of the host lattice and characteristics of the copper ions. The X-ray study indicates disorder of a water molecule (O(3)) and a large anisotropic thermal ellipsoid for another (O(5)) at 150 K. The thermal parameters of the water molecule O(3) is large at 298 K. We interpret these results as a dynamical disorder of an oxygen atom and water protons in pure Zn(D,L-histidine)$_2$ at high temperatures. These positions are frozen in specific disordered sites at low T. The peak in the specific heat between 240 and 268 K would indicate the temperature range where this transition takes place. Quantitative specific heat measurements and also proton NMR studies should prove this hypothesis.[55]

The EPR spectra of the copper ions also reflect the dynamical disorder of the pure lattice. A peak in the EPR line width occurring in the same temperature range as the peak in the specific heat of the pure compound (Figure 12) is attributed to the freezing of the dynamical disorder. It proves the interrelation of the two processes, which we emphasize in the analysis of the data. The order parameter $\xi(T)$, defined in terms of the temperature variation of the spectrum, is assigned to a property of pure Zn(D,L-histidine)$_2$. We do not have an specific explanation on the empirical sigmoidal temperature variation observed (eq 12), but the concept is simple and useful to tabulate $\xi(T)$. The cooperative atom dynamics proposed here contrasts with the picture of an independent dynamics, where the populations of the levels follow a Boltzmann distribution. Other authors[12] interpreted temperature dependences of the EPR spectra in other compounds with Boltzmann factors, using temperature-dependent energy levels.

We assume that Cu ions replace Zn ions in the host lattice. Even if the compound contains a racemic mixture of histidine, the metal ions (Zn or Cu) are bonded to two L-histidine (or two D-histidine) molecules, as in biological molecules. As a consequence of the Jahn−Teller theorem, the C_2 symmetry of the Zn sites is lost at the copper ions and we observe at low temperature two possible states geometrically related by a C_2

rotation around ***b***. The EPR data indicates that the configuration around the copper ion in these lower energy states have axial symmetry and suggest that one of the amine N(1) ligands is displaced away from the copper ion, and the three other nitrogen ligands are approximately in the perpendicular plane. This configuration is sketched in Figure 13a for the two distorted copper sites. The double-well potential shown in Figure 13a should hold at the copper ions for the positions of the amine nitrogen ligands to copper and the concomitant displacements of other ligands.

The EPR data has been analyzed at two levels. A two-states model for the motional narrowing and collapse explains the main experimental findings: the collapse of the two spectra observed at low temperature to a single averaged spectrum in a sharp transition at a temperature T_c, and the variation of the line width with hyperfine component. A more detailed four-states model explains these and other observations with higher precision adding two additional excited states that are populated at high temperatures. These states introduce contributions needed to explain the data for **B** along the ***b***-axis and in the *ac* plane, where the simpler two-states model fails to predict the observed changes. The four-states model assumes that the dynamics of the ligands to copper is linked to the dynamics of the oxygen and protons of a water molecule observed in pure Zn(D,L-histidine)$_2$ in the X-ray and specific heat measurements. The displacements of the individual ligands to the metal ion at the copper ion sites are, however, different than those in the pure lattice. This is because dynamical Jahn−Teller distortions, existing for copper but not for zinc ions, lower the point symmetry of the metal. Our data show that the dynamics of the local distortions is driven by the collective disorder of the lattice. They also show that the dynamics of the disorder does not change appreciably between protonated and deuterated samples. The relatively high activation energy $\Delta E^* = 1000$ K obtained from the four-states model produces slow hopping rates at low temperatures and allows viewing at 268 K the transition from the regime of two separate copper spectra to the collapsed regime, where only one copper spectrum is observed. This value of ΔE^* reflects a property of the dynamics of pure Zn(D,L-histidine)$_2$, which drives the vibronic coupling of the copper ions with a Jahn−Teller mode at the position of the impurity.

The structure proposed for states I and II reminds us of the structure of the copper sites normally observed in type 1 blue copper proteins, particularly plastocyanin.[13,56−58] In those cases the Cu(II) ion is bonded to two imidazole N_δ from histidine residues, and to two S, one from a cysteine and the other from a methionine residue. The Cu−S_{met} distance is quite long (∼2.8 Å), and the copper ion is in an elongated C_{3v} distorted tetrahedral geometry where the (approximate) C_3 symmetry axis is the Cu−S_{met} direction, and the copper ion is displaced toward the opposite trigonal plane.[56,57] The large structural deviation from the energetically favored square planar or square pyramidal geometries is attributed to a strain enforced by the surrounding polypeptide chains. This distortion facilitates the function of the protein by favoring the approach to the transition state of the electron-transfer reaction Cu(II)/Cu(I).

In the model proposed here to explain the data for Cu:Zn-(D,L-histidine)$_2$ the tetrahedral structure around copper would be produced by the host lattice trying to stabilize the natural bonding scheme of the Zn ions. The trigonal distortion appears as a consequence of the Jahn−Teller theorem, dynamical at high temperature but static at low temperature. In comparison with the previous case, we replace the S ligands by the amine N of the histidines. The Jahn−Teller distortion involves an increase of the distance between Cu and one amine N(1) ligand, which reduces the energy of the distorted state of the Cu ion from that of the undistorted state. At low temperature these axially distorted states are frozen in, and it is possible to observe their EPR spectrum. The reduction in the hyperfine splitting parameter in the direction of the symmetry axis ($A_{||}$) characteristic of the EPR spectra of type 1 blue copper protein, is due to the highly covalent S_{Cys} equatorial bond[56,57] and does not occur in Cu:Zn(D,L-histidine)$_2$. ENDOR and ESEEM data on Cu ions in Zn-(D,L-histidine)$_2$ would allow to obtain more information about the bonding scheme, to verify the proposed model.

Colaneri and Peisach[28] reported a single-crystal EPR and ESEEM analysis of Cu(II)-doped bis(L-histidinato)cadmium dihydrate. At 77 K they observe two copper sites, when only one should be observed if copper ions replace Cd ions according to the crystallographic information.[17] From these low *T* data they propose a binding site for the copper ion. The bonding scheme proposed here for Cu ions in Zn(D,L-histidine)$_2$ is different than that proposed for Cd(L-histidine)$_2$(H_2O)$_2$. At room temperature Colaneri and Peisach[28] observe a single copper site, with EPR parameters that are the average of the values obtained at 77 K. The room temperature behavior was attributed to a dynamical averaging of the spectra of the low-temperature sites, produced by a hopping of the copper ions between them. This situation is similar to the one proposed here for Cu:Zn(D,L-histidine)$_2$. Since they do not include in their publication the single-crystal EPR data at room temperature, we cannot make a detailed comparison of the results in both systems. Colaneri and Peisach[28] did not report a dependence of the line width on hyperfine component.

Variations of the line width with hyperfine component have been observed in the *g*-parallel region of the EPR spectra of frozen solution or powder samples of several copper compounds by Lewis et al.[59] and by Froncisz and Hyde.[60,61] A broadening mechanism in terms of correlated distributions of molecular bonding parameters was proposed to explain the experimental results[60] and have been extensively used in the study of copper spectra, particularly in biologically active cupric ions.[62] The dynamical mechanism proposed here to explain the unequal line widths of the hyperfine components of Cu(II) in Zn(D,L-histidine)$_2$ offers an alternative explanation for the observed selective broadening. It produces similar effects and is clearly observed in the spectra of frozen solutions and powder samples as shown in this work. More measurements of the temperature dependence of the spectra in other systems may be helpful to clarify this point.

Acknowledgment. We are grateful to Drs. Daniel Rodrigues, Mario Passeggi, and Alejandro Vila for helpful discussions. This work was supported by grants CAI+D from Universidad Nacional del Litoral, PIP 4807 from the Consejo Nacional de Investigaciones Científicas y Técnicas (CONICET) of Argentina and by Fundación Antorchas. S.D.D. had a fellowship of CONICET. R.C. is a fellow of CONICET.

Supporting Information Available: The results of our crystallographic study at 293 and 150 K are contained in the following tables: crystal data and structure refinement for Zn-(D,L-histidine)$_2$ (Table S1); fractional atomic coordinates and equivalent isotropic parameters for all non-hydrogen atoms (Table S2); listings of atomic anisotropic thermal parameters (Table S3); hydrogen atoms positions (Table S4); bond lengths and angles (Table S5); hydrogen bonds lengths and angles (Table S6). This material is available via the Internet at http://pubs.acs.org.

References and Notes

(1) Abragam, A.; Bleaney, B. *Electron Paramagnetic Resonance of Transition Ions*; Oxford University Press: London, 1970.

(2) Fujimoto, M. *The Physics of Structural Phase Transitions*; Springer: Berlin, 1997; Chapters 8 and 9.

(3) Bersuker, I. B. *Electronic Structure and Properties of Transition Metal Compounds. Introduction to the Theory;* Wiley: New York, 1996.

(4) Bleaney, B.; Ingram, D. J. E. *Proc. R. Soc. Ser. A* **1950**, *63*, 408.

(5) O'Brien, M. C. M. *Proc. R. Soc. London A* **1964**, *281*, 323.

(6) Ham, F. S. In *Electron Paramagnetic Resonance*; Geschwind, S., Ed.; Plenum: New York, 1972; p 1.

(7) Silver, B. L.; Getz, D. *J. Chem. Phys.* **1974**, *61*, 638.

(8) Bersuker, I. B. *The Jahn−Teller Effect and Vibronic Interactions in Modern Chemistry*; Plenum: New York, 1984.

(9) Riley, M. J.; Hitchman, M. A.; Reinen, D. *Chem. Phys.* **1986**, *102*, 11.

(10) Riley, M. J.; Hitchman, M. A.; Mohammed, A. W. *J. Chem. Phys.* **1987**, *87*, 3766.

(11) Bebendorf, J.; Bürgi, H. B.; Gamp, E.; Hitchman, M. A.; Murphy, A.; Reinen, D.; Riley, M. J.; Stratemeier, H. *Inorg. Chem.* **1996**, *35*, 7419.

(12) Hoffmann, S. K.; Goslar, J.; Hilczer, W.; Agustyniak, M. A.; Marciniak, M. *J. Phys. Chem*. **1998**, *102*, 1697.

(13) Lippard, S. J.; Berg, J. M. *Principles of Bioinorganic Chemistry*; University Science Books: Mill Valley, CA, 1994.

(14) Harding, M. M.; Cole, S. J. *Acta Crystallogr*. **1963**, *16*, 643.

(15) Weitzel, G.; Schneider, F.; Fretzdorff, A. M.; Heyke, H. E. *Hoppe-Seyl. Z.* **1957**, *307*, 14. Kretsinger, R. H.; Cotton, F. A.; Bryan, R. F. *Acta Crystallogr*. **1963**, *16*, 651. Candlin, R.; Harding, M. M. *J. Chem. Soc. A* **1967**, 421. Kistenmacher, T. J. *Acta Crystallogr. B* **1972**, *28*, 1302.

(16) Harding, M. M.; Long, H. A. *J. Chem. Soc. (A)* **1968**, 2554. Candlin, R.; Harding, M. M. *J. Chem. Soc. (A)* **1970**, 384.

(17) Candlin, R.; Harding, M. M. *J. Chem. Soc.* **1967**, 421. Fuess, H.; Bartunik, H *Acta Crystallogr. B* **1976**, *32*, 2803.

(18) Frazer, K. A.; Harding, M. M. *J. Chem. Soc A* **1967**, 415. Sakurai, T.; Iwasaki, H.; Katano, T.; Nakahashi, Y. *Acta Crystallogr. B* **1978**, 34, 660. Shvelashvili, A. E.; Zedelashvili, E. N.; Beshkenadze, I. A.; Svanidze, O. P.; Miminoshvili, E. B.; Koberidze, N. A. *Soobshch. Akad. Nauk. Gruz. SSR* **1984**, *116*, 521.

(19) Evertsson, B. *Acta Crystallogr. B* **1969**, *25*, 30. Camerman, D. N.; Fawcett, J. K.; Kruck, T. P. A.; Sarkar, B.; Camerman, A. *J. Am. Chem. Soc*. **1978**, *100*, 2690.

(20) Takeda, K.; Arata, Y.; Fujiwara, J. *J. Chem. Phys*. **1970**, *53*, 854. Fujimoto, M.; Janecka, J. *J. Chem. Phys*. **1971**, *55*, 1152. Fujimoto, M.; Wylie, L. A.; Saito, S. *J. Chem. Phys*. **1973**, *58*, 1273.

(21) Hirasawa, R.; Kon, H. *J. Chem. Phys.* **1972**, *56*, 4467.

(22) Calvo, R.; Oseroff, S. B.; Abache, H. C. *J. Chem. Phys.* **1980**, *72*, 760.

(23) Rockenbauer, A.; Györ, M.; Szabó-Plánka, T. *J. Chem. Phys.* **1987**, *86*, 976.

(24) Steren, C. A.; Calvo, R.; Piro, O.; Rivero, B. E. *Inorg. Chem.* **1989**, *28*, 1933.

(25) Colaneri, M. J.; Potenza, J. A.; Schugar, H. J.; Peisach, J. *J. Am. Chem. Soc.* **1990**, *112*, 9451.

(26) Colaneri, M. J.; Peisach, J. *J. Am. Chem. Soc.* **1992**, *114*, 5335.

(27) Brondino, C. D.; Casado, N. M. C.; Passeggi, M. C. G.; Calvo, R. *Inorg. Chem.* **1993**, *32*, 2078.

(28) Colaneri, M. J.; Peisach, J. *J. Am. Chem. Soc.* **1995**, *117*, 6308.

(29) Dalosto, S. D.; Calvo, R.; Piro, O. E.; Castellano, E. E. *J. Inorg. Biochem.* **1999**, *77*, 155.

(30) Massa, M. B.; Dalosto, S. D.; Ferreyra, M. G.; Labadie, G.; Calvo, R. *J. Phys. Chem. A* **1999**, *103*, 2606.

(31) *International Tables for X-ray Crystalography*: *Vol. A, Space Group Symmetry*; Kynoch Press: Birmingham, UK, 1974; Vol. I, p 101.

(32) Sheldrix, G. M. Shelxs86, *Program for the Solution of Crystal Structures;* University of Göttingen: Göttingen, Germany, 1985.

(33) Sheldrix, G. M. Shelxl93, Program for the Refinement of Crystal Structures; University of Göttingen, Germany, 1993.

(34) Spek, A. L. PLATON94, Program for the automated analysis of molecular geometry; University of Utrech, The Netherlands, 1994.

(35) Isaacson, R. A.; Lulich, C.; Oseroff, S. B.; Calvo, R. *Rev. Sci. Instrum.* **1980,** *51*, 109.

(36) Feher, G. *Bell Syst. Techn. J.* **1957**, *36*, 449.

(37) Weil, J. A. *J. Magn. Reson.* **1975**, *18*, 113.

(38) Weil, J. A.; Bolton, J. R.; Wertz, J. E. *Electron Paramagnetic Resonance. Elementary Theory and Practical Applications*; Wiley: New. York, 1994, Ch. 6.

(39) Weger, M. *Bell Syst. Techn. J.* **1960**, *39*, 1013.

(40) Simulations of the spectra observed with the magnetic field applied in symmetry-related orientations allow to estimate 50 ± 5% populations for each site.

(41) Anderson,P. W. *J. Phys. Soc. Jpn.* **1954**, *9*, 316.

(42) Clough, S.; Hill, J. R. *J. Phys. C: Solid State Phys.* **1975**, *8*, 2274.

(43) Bang, L. S.; Buisson, R.; Williams, F. I. B. *J. Phys.* **1974**, *35*, 49.

(44) Hoffmann, S. K.; Goslar, J. *Acta Phys. Polon.* **1979**, *55*, 471.

(45) Gill, J. C. *J. Phys. C* **1975**, *8*, 4203.

(46) Sack, R. A. *Mol. Phys*. **1958**, *1*, 163.

(47) Abragam, A. *The Principles of Nuclear Magnetism*; Oxford University Press: London, 1961.

(48) Blume, M. *Phys. Rev.* **1968**, *174*, 351.

(49) Hopping is a fast dynamical process that does not depend on the nuclear spin orientation.

(50) Tinoco, I.; Sauer, K.; Wang, J. C. *Physical Chemistry. Principles and Applications in Biological Sciences*; Prentice Hall: Upper Saddle River, 1995; Chapter 7.

(51) Riley, M. J.; Hitchman, M. A.; Mohammed, A. W. *J. Chem. Phys.* **1987**, *87*, 3766.

(52) Astley, T.; Headlam, H.; Hitchman, M. A.; Keene, F. R.; Pilbrow, J.; Stratemeier, H.; Tiekink, E. R. T.; Zhong, Y. C. *J. Chem. Soc., Dalton Trans*. **1995**, 3809.

(53) We assume that the effective mass of the N(2) imidazole nitrogens (related to the mass of the imidazole ring) is larger, and consequently these ligands are more difficult to move.

(54) Jahn, H. A.; Teller, E. *Proc. R. Soc.* **1937**, *A161*, 220.

(55) NMR and detailed specific heat measurements performed by P. R. Levstein et al. (to be published) would prove this assumption.

(56) Solomon, E. I.; Baldwin, M. J.; Lowery, M. D. *Chem. Rev.* **1992**, *92*, 521.

(57) Holm, R. H.; Kennepohl, P.; Solomon, E. I. *Chem. Rev.* **1996**, *96*, 2239.

(58) Kaim, W.; Rall, J. *Angew. Chem., Int. Ed. Eng*. **1996**, *35*, 43.

(59) Lewis, W. B.; Alei, M.; Morgan, L. O. *J. Chem. Phys.* **1966**, *44*, 2409.

(60) Froncisz, W.; Hyde, J. S. *J. Chem. Phys*. **1980**, *73*, 3123.

(61) Hyde, J. S.; Froncisz, W. *Annu. Rev. Biophys. Bioeng*. **1982**, *11*, 391.

(62) Aqualino, A.; Brill, A. S.; Bryce, G. F.; Gerstman, B. S. *Phys. Rev. A* **1991**, *44*, 5257.